JES Focus Issue on Advances in Modern Polymer Electrolyte Fuel Cells in Honor of Shimshon Gottesfeld

# Enhanced Water Removal from PEM Fuel Cells Using Acoustic Pressure Waves

**Mehdi Mortazavi,[*,z] Anthony D. Santamaria,[*] Jingru Z. Benner, and Vedang Chauhan**

*Department of Mechanical Engineering, Western New England University, Springfield, Massachusetts 01119, USA*

Liquid water management remains a primary challenge in developing next generation low temperature proton exchange membrane fuel cells. This work demonstrates the use of acoustic pressure waves superimposed on reactant channel air flow as an effective means to enhance liquid water removal from gas diffusion layer surfaces. Experiments were conducted for a range of acoustic vibration frequencies; 20 to 120 Hz with 20 Hz intervals. Water transport was visualized using a CCD camera mounted over a transparent ex-situ PEM fuel cell test channel. Cumulative water areas were measured along the flow channel along with two-phase flow pressure drop for water fluxes of 400, 600, and 800 $\mu\ell/h$ and a superficial air velocity of 1.82 m/s. Results show that superimposing acoustic pressure waves on the air flow can reduce liquid water build up and, therefore, reduce two-phase flow pressure drops. Cumulative water area was reduced almost 85% with an acoustic vibration frequency of 80 Hz compared to the 0 Hz case. Additionally, at 80 Hz the lowest two-phase flow pressure drop was recorded. Finally, a comparison of energy usage is made between different acoustic vibration application methods.

 [DOI: 10.1149/2.0211907jes]

Manuscript submitted January 7, 2019; revised manuscript received March 28, 2019. Published April 17, 2019. *This paper is part of the JES Focus Issue on Advances in Modern Polymer Electrolyte Fuel Cells in Honor of Shimshon Gottesfeld.*

Proton exchange membrane (PEM) fuel cells are considered a viable alternative to internal combustion engines due to their high volumetric power density and zero source greenhouse gas emission.[1–6] During the oxygen reduction reaction in the cathode side of a PEM fuel, water is produced as a by-product. Efficient and reliable operation of the cell requires a uniform and continuous supply of reactants across the electrodes. Therefore, the produced water should be carefully managed to avoid flooding issues within the cell. This is because while the membrane ionic conductivity requires adequate hydration, an excess amount of water can block the transport of reactant gases to the catalyst layer which causes fuel starvation and increase overpotential.[7–9] Flooding in PEM fuel cells has been extensively investigated in multiple studies.[10–15] In addition to lower cell performance, the accumulation of excess water in a PEM fuel cell can cause concerns with respect to freeze/thaw damage,[16] start-up conditions,[17,18] and component degradation.[19]

Many studies have investigated water transport through the porous electrode structure.[20–40] Bazylak et al.[32] studied the dynamics of liquid water transport through the GDL by fluorescence microscopy and observed that water emerges from the surface of the GDL at some preferential locations. These preferential locations were reported to change intermittently which is an indication of interconnected water pathway within the GDL. They also reported that water accumulation within the flow channel increases due to pinning and the formation of water slugs near the breakthrough locations.

Water transport phenomena on the surface of the GDL and within the flow channels of the PEM fuel cell has also been investigated throughout literature.[41–46] Zhang et al.[41] conducted in-situ experiments to study liquid water transport in the flow channels of a PEM fuel cell and observed that water removal occurs by different mechanisms, depending on the gas flow rate and water production rate. For water removal rates less than the water production rate, a water lens may form within the gas channel which can ultimately clog the flow channel as it grows in size. For high superficial gas velocities within the flow channel, the shear force of the core gas flow can detach water droplet from the surface of the GDL and form mist flow in the flow channel. Another transport mechanism occurs when water wicks onto the hydrophilic channel walls and forms annular film flow and/or slug flow in the channel. The Concus-Finn condition defines the criteria for liquid wicking into a corner. When the static contact angle is less then $\pi/2 - \alpha$, where $\alpha$ is the corner half-angle, a critical wetting condition is met and liquid wicks to the corner.[47,48] At low temperatures and/or high current densities, more water accumulates within the flow channel which can lead to channel flooding. Water transport in flow channels of a PEM fuel cell is categorized as capillary-scale transport phenomena with a characteristic length defined by a Bond number less than one. The Bond number, which is a ratio of gravitational acceleration effects to surface tension effects on a liquid-vapor interface, is defined as $Bo = (L/L_c)^2$ where L is the characteristic length and $L_c$ is the capillary length. The capillary length, also referred to as the Laplace length, is defined as $L_c = \sqrt{\sigma/\rho g}$, where $\sigma$ is the surface tension, $\rho$ is the liquid density, and g is the gravitational acceleration. Due to the small characteristic length scale associated with the PEM fuel cell it can be concluded that the gravity's impact on the liquid-gas two-phase flow is insignificant. However, the surface tension effects are dominant and strongly influence the transport phenomena in PEM fuel cells. Other than the liquid inertial and wall shear stress that restrain the droplet motion, contact line pinning and contact angle hysteresis restrain water movement in the flow channel of a PEM fuel cell. The pinning of a contact line results in a change in shape of the liquid surface in order to accommodate pressure, gravitational, and shear forces without any bulk motion of the droplet. The difference between advancing and receding static contact angles at the onset of motion is referred to as contact angle hysteresis. This property causes a droplet to distort on the surface of the GDL without moving.[49]

While the majority of literature focused on *passive* methods of removing water from the flow channels of the PEM fuel cell, few studies investigated on the *active* methods. In this context, the passive water removal methods refer to water removal from the flow channels through capillary wicking to corners of the flow channel, shear stresses and pressure differences generated by reactant flow, and/or liquid water evaporation by the gas stream. In contrast to passive methods of water removal, the active water removal schemes refer to methods that facilitate water removal by an external excitation.

Palan et al.[50] theoretically studied excess water removal from flow channels of PEM fuel cells by utilizing vibro-acoustic methods. They studied the effects of applying flexural waves, acoustic waves, and surface waves to a stack of PEM fuel cell and compared them based on the minimum vibration energy required to remove each droplet. They reported that a 2-mm radius water droplet can be removed from flow channels of a PEM fuel cell with parasitic power requirement as

*Electrochemical Society Member.
zE-mail: mehdi.mortazavi@wne.edu

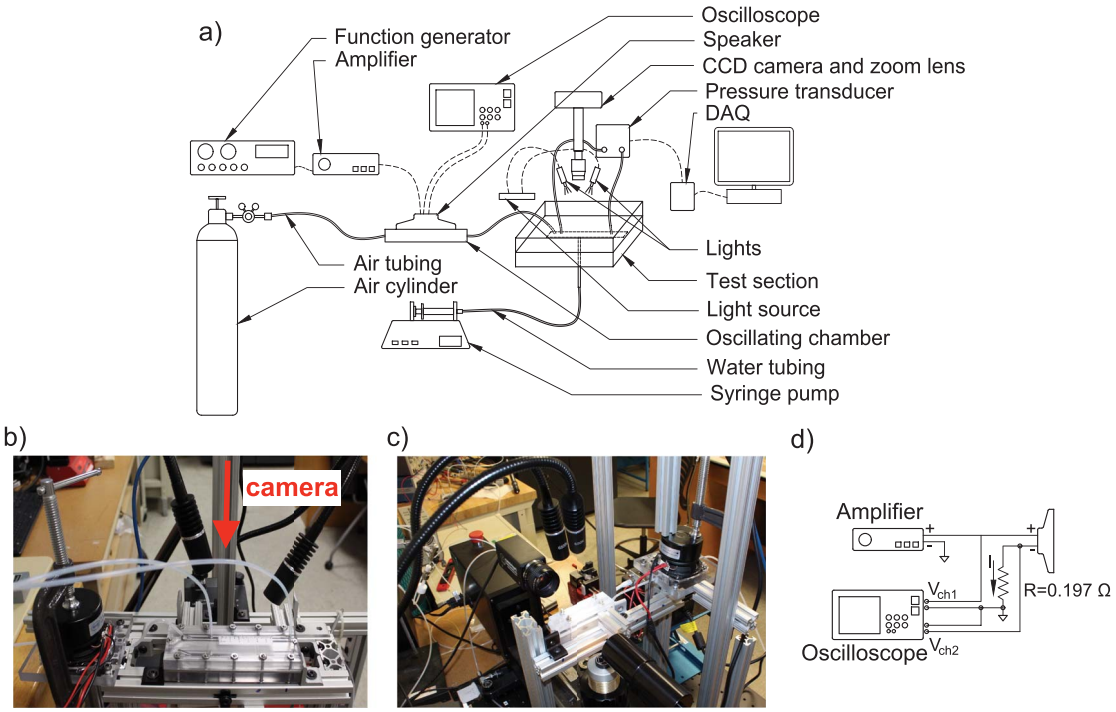


**Figure 1.** (a) Schematic of the experimental setup, (b) test section used for visualizing water accumulation, (c) test section used in goniometer, (d) wiring diagram for monitoring speaker power.

low as 21 mW. By comparing the three methods, they concluded that applying surface acoustic wave is the most efficient method in terms of energy utilization to remove water droplets. In a similar approach, Schafer and Allen[51] superimposed acoustic pressure waves on gas flow to remove liquid water droplets in an ex-situ test section. They excited the liquid surfaces at their natural frequencies and were able to remove water droplets from the flow channel with gas flow rates much lower than the cases without acoustic excitation. While the use of acoustic and/or mechanical vibration in removing and/or transporting water build up is extensively investigated for a variety of industrial applications,[53–56] few attention has been paid to apply this method in PEM fuel cells in order to alleviate flooding issues.

In this work, an enhanced water removal technique from a flow channel of an ex-situ PEM fuel cell is studied by exciting water droplets at their natural frequencies. By doing so, resonance can be induced in water droplets which facilitates their removal from the flow channel. Acoustic pressure waves are superimposed on air flow prior to entering the ex-situ test section and water removal is visualized at different acoustic frequencies. The effect of superimposing acoustic pressure waves on water transport in the flow channel is studied by visualizing the flow channel from the top-view with a CCD camera. Images are then processed to obtain water accumulation in the flow channel at different frequencies. Different patterns of superimposing acoustic vibration is used as discussed in Experimental procedure section. In addition to water accumulation, liquid water droplet oscillation is investigated under the influence of acoustic pressure wave from a side-view angle in a goniometer. The liquid-gas two-phase flow pressure drop, a property that describes the amount of liquid water accumulation within the flow channel, is also measured along the length of the flow channel. Finally, the parasitic power to expel water based on each superimposition scheme is studied.

## Experimental

Water removal from ex-situ PEM fuel cell test sections was studied in two different apparatus. In one apparatus, water accumulation in a flow channel was monitored along 27 mm length of the channel. In the other apparatus, droplet oscillation during its growth on the surface of the GDL was observed from a side-view angle. Fig. 1a shows the schematic of the experimental setup used to study water accumulation in the channel. Fig. 1b shows the test section used for water accumulation experiments. For oscillation studies, a goniometer (ramé-hart, 295-U1) was used along with an ex-situ test section that allowed side-view visualization, as shown in Fig. 1c. In the experimental setup, a function generator (33120A, Hewlett Packard) was used to generate sine waves at different frequencies between 20 to 120 Hz and with a 20-Hz increment. The sine waves were then amplified in an amplifier and were transferred to the speaker in the oscillator chamber. A syringe pump was used to inject water at different flow rates to the back side of the GDL in the test section. A pressure transducer measured liquid-gas two-phase flow pressure drop along 9 cm of the flow channel. The pressure transducer had an operating range between 0 and 500 Pa and an accuracy of ±2.5 Pa (Omega, PX653 02D5V). Pressure measurements were done at sampling frequencies of 100, 200, or 240 Hz, depending upon the flow conditions. The pressure transducer communicated with a data acquisition system which communicated with a VI code developed in LabView. A CCD camera (Thorlabs, 1501M-USB) recorded water emergence, growth, and transport within the flow channel. The camera was equipped with a zoom lens (MVL6X12Z) and a 0.67X adapter (MVL067A) to provide a 800 × 1040 pixel resolution over a 20.9-mm (W) × 27.2-mm (L) field of view. This is equivalent to a spatial resolution of 26.1 μm/pixel. Two 6-W adjustable intensity LED lights were used to provide the required illumination. Table I lists the experimental conditions of this study. The superficial velocity listed in this table is the bulk velocity of the fluid at the cross-sectional area of the flow channel. Air was passed through an oscillator chamber prior to entering into the apparatus to superimpose acoustic pressure wave. In the chamber, a 15-W speaker was installed above a 75-mm diameter circular chamber with four screws. The depth of the chamber was 8 mm. Air entered into the chamber through a 1/8-inch opening in one side and was exposed to the speaker within the chamber. The acoustically superimposed air was then delivered to the test section through a 10-cm-long, 1/8 inch PTFE tube. Adhesive sealant was applied in the interface between the speaker and the chamber to air-tight the oscillator chamber. The power of the speaker was carefully monitored based on the two voltages measured by an oscilloscope (TDS

**Table I. Experiment conditions.**

| | Accumulation study (top-view) | Oscillation study (side-view) |
|---|---|---|
| overall channel length | 128 mm | 100 mm |
| length of field of view | 27 mm | 4.8 mm |
| length of pressure measurement | 90 mm | NA |
| channel width | 3 mm | 5mm |
| channel depth | 2.4 mm | 4.5 mm |
| air flow rate | 788 mℓ/min | 1755, 2457, 3105 mℓ/min |
| water flow rate | 400, 600, 800 μℓ/h | 2000 μℓ/h |
| superficial air velocity | 1.82 m/s | 1.30, 1.82, 2.30 m/s |
| superficial water velocity | $9.25\times10^{-4}$, $1.38\times10^{-3}$, $1.82\times10^{-3}$ m/s | $1.48\times10^{-3}$ m/s |
| air Reynold number | 319.2 | 405, 567, 717 |
| water Reynolds number | 2.76, 4.14, 5.52 | 7.85 |

1012, Tektronix) according to the wiring diagram shown in Fig. 1d. All experiments were conducted at 4.75 W speaker power.

As a common practice, GDLs are treated with PTFE for an improved liquid water transport.[57] In this study 8 wt% PTFE treated Toray carbon papers were used as GDL samples. The samples were treated in-house based on the procedure explained in Ref. 58. To briefly explain, untreated GDL samples were first dipped in the PTFE emulsion (60 wt% dispersion in $H_2O$, ALDRICH) for 10 h. The substrates were then put in a furnace at 120°C for 1 h. According to Ref. 58 in order to make a uniform PTFE distribution through the GDL, the temperature of the furnace was then increased to 360°C for another 1 h.

***Test sections.***—Two different test sections were used in this study for top-view and side-view of the flow channel. The test section used to monitor water accumulation within the flow channel from the top-view had a 128-mm-long, 3-mm-wide flow channel machined on a 2.4-mm-thick aluminum plate. The aluminum plate was sandwiched between two polycarbonate plates via twelve 1/8 inch screws. From one polycarbonate plate, air was supplied to the flow channel through an inlet port machined at 45° with respect to the flow channel. Water was injected to the back side of the GDL from the other polycarbonate plate and through a stainless steel capillary with 125 μm inside diameter (U-156, Upchurch). The interfaces between the aluminum plate and polycarbonate plates were sealed with o-ring cords inserted in grooves around the GDL. The o-ring groves were machined on the polycarbonate plate.

In an actual PEM fuel cell, the flow channels are typically around 1 mm on each side while the flow channel used in this study was larger than that. This is because the objective of this study is to quantitatively evaluate the effects of acoustic pressure wave on water removal from the surface of the GDL. Although channel walls can affect water transport mechanism, this study focuses on droplet oscillation and removal induced by acoustic pressure waves at frequencies close to the natural frequency of the water droplets. Therefore, the flow channel used in this study was a scaled-up to ensure absence of wall effect. This study, however, can be a basis for a more realistic case of actual channel size.

Water droplet oscillation during its growth on the surface of the GDL was studied with another test section that allowed visualization from a lateral direction. The flow channel of this test section was formed by four pieces of polycarbonate plates screwed to each other. The width of the flow channel was 5 mm and its height was 4.5 mm. Similar to the top-view test section, a larger channel size was used in the side-view test section in order to avoid droplet contact with the side walls. Air from the oscillating chamber was supplied into the inlet of the test section and water was injected to the back side of the GDL through a 125μm capillary tube.

***Experimental procedure.***—Experimental runs were conducted for 600 or 3600 s after the emergence of the first droplet from the surface of the GDL. For each run, a new PTFE-treated GDL sample was used in the test section. In addition to runs with no acoustic vibration (speaker off), experiments were conducted for different experimental patterns of (i) speaker on, (ii) speaker oscillating on/off, and (iii) speaker on demand. In runs tagged with speaker on, the speaker was kept on throughout the entire experiment. For runs tagged with speaker on/off, a timer outlet was used to turn the function generator on and off with 10 s intervals. Therefore, in these runs the speaker only operated half of the experiment duration. Finally, runs tagged with speaker on demand represent conditions at which the speaker was mainly off but was turned on manually once a water droplet was formed on the surface of the GDL.

***Image processing.***—A CCD camera captured water transport within the flow channel at 12 frames per second rate. The images were then analyzed to obtain liquid water coverage area in the flow channel. The image processing was done based on image filtering, segmentation using thresholding, and connected component analysis through the computer vision techniques. First, a mask image the size of the input image was created with flow channel details as white pixels and the background details as black pixels. Once the mask image was created, the background was subtracted in order to remove the stationary details from the image. This was followed by a noise removal step to eliminate the noise resulting from slight variations in illumination, minor workbench vibrations, and motion blur. The resulted image was converted to a binary image by using thresholding. The binary images were then processed to calculate the white pixel total which in fact represents water droplets in the flow channel.

## Results and Discussion

***Channel images.***—Channel images were recorded at 12 frames per second to monitor water accumulation within the flow channel. Fig. 2 shows images of the flow channel during 600 s after the first emergence of water droplet. For purpose of brevity, only a limited set of images are shown. In all images, the direction of air flow was from top to bottom. Fig. 2 also shows a raw image which includes the flow channel, highlighted with a blue box, and its surrounding. Water emergence occurred around 0 cm on the ruler. The superficial air velocity was 1.82 m/s and water was injected at 400 μℓ/h. The processed images for different acoustic frequencies are shown in this figure. Images on the first row belong to an experiment without acoustic vibration. It can be observed from Fig. 2 that water accumulation for an experiment without acoustic vibration is the greatest compared to other runs. The lowest water accumulation is observed for 80 Hz. The first image at this frequency shows a water droplet pinned to channel wall 18 mm downstream of the emergence point. However, the flow channel image at 120 s does not show this droplet, an indication that the droplet has been expelled from the field of view. Other images for this frequency also show water droplets only at the emergence point. For runs conducted at 80 Hz, it was observed that droplets tend to detach from the surface of the GDL few seconds after emergence, once their area reached $3.11 \pm 0.48$ mm$^2$.

***Water accumulation.***—In order to study the effect of superimposing acoustic pressure wave on water removal from the flow channel,

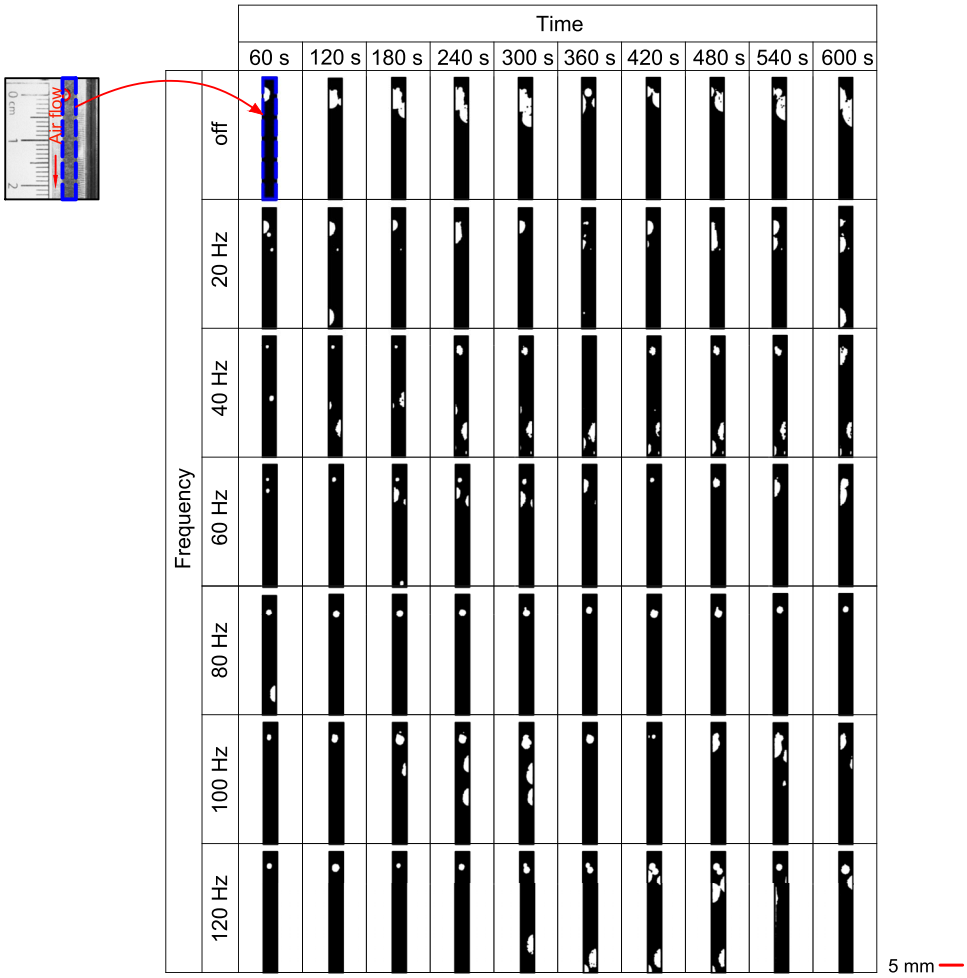


**Figure 2.** Visualizing water transport in the flow channel for superficial air velocity of 1.82 m/s, water injection rate of 400 $\mu\ell$/h, and at different acoustic vibrations. The raw image belongs to an experiment with no acoustic vibration and 60 s after the emergence of water droplet from the surface of the GDL. The blue boxes highlight the flow channel. Processed images are shown at different times and frequencies.

the cumulative area of water droplet was defined as:

$$\text{cumulative area at time t} = \sum_{i=1}^{t} \text{area of water droplet in image at time t}$$

where $i$ is the number of image at 0.5 s time interval after the first emergence. Although the cumulative area only compares the surface area covered by the droplet and does not take into consideration the height of the water droplet, this property can still be used for a basic comparison. Further comparison in accumulated water volume can be done by analyzing the two-phase flow pressure drops as discussed in Two-phase flow pressure drop section. Fig. 3a shows the cumulative area of the water droplets in the field of view of the camera. The cumulative areas are shown for each 20 s of the experiment. Each data point

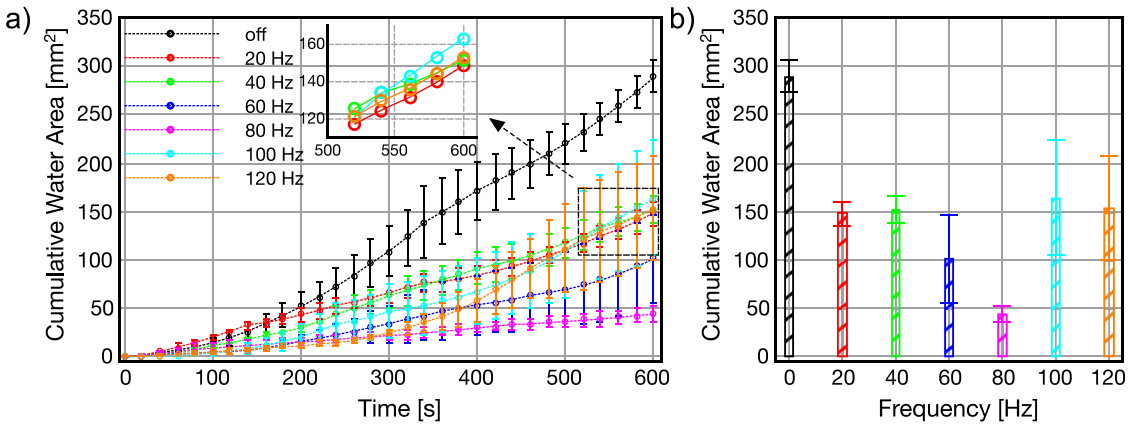


**Figure 3.** (a) Cumulative area of water droplets. Experiments were conducted at 400 $\mu\ell$/h water flow rate and 1.82 m/s superficial air velocity. (b) cumulative area at 600 s.

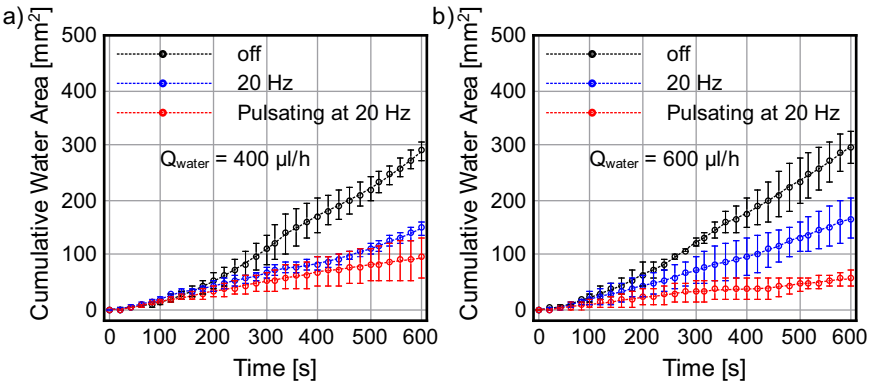


**Figure 4.** Comparison of cumulative area of water droplet for speaker off, speaker on, and pulsating the speaker on and off with 10 s time intervals. The superficial air velocity was 1.82 m/s. (a) water flow rate of 400 $\mu\ell$/h and (b) water flow rate of 600 $\mu\ell$/h.

is based upon the average of three measurements and the error bars represent the calculated standard deviation. For each run, 1200 images were processed over 600 s of the experiment. Similar to observation from Fig. 2, Fig. 3a shows that water accumulation in the field of view is greatest when the speaker was off. However, the figure shows that superimposing acoustic pressure wave on air can enhance water removal from the flow channel. While the average cumulative area of water droplets reach 288.6 mm$^2$ for runs without acoustic vibration, the figure suggests that this average can be as low as 43.9 mm$^2$ for runs with speaker operating at 80 Hz. In addition, the figure shows that other frequencies (20, 40, 60, 100, 120 Hz) resulted in less water accumulation compared to runs without acoustic vibration. However, water accumulations were still greater than runs conducted at 80 Hz. Fig. 3b shows the overall cumulative area at the end of experiments. Fig. 3a shows that superimposing acoustic pressure wave at 60 Hz can enhance water removal with respect to the other four frequencies (20, 40, 100, and 120 Hz) but is not as efficient as 80 Hz. The overall cumulative area of four frequencies of 20, 40, 100, and 120 Hz were almost identical as shown in the figure in the inset and Fig. 3b. The overall cumulative area shown in this figure suggests that although water accumulation under 20, 40, 100, and 120 Hz are almost identical, the standard deviation for 100 and 120 Hz are larger than that for 20 and 40 Hz. The larger standard deviation for higher frequencies can be justified by water pinning to the channel side walls in some of the runs. As water droplets pin to the channel side walls, an accumulation site forms which increases in size over time.[32] As water droplets increase in size, their natural frequency decrease and therefore, the higher frequencies used in this study (100 and 120 Hz) were not capable of removing water more efficiently from the field of view. Runs with water droplets pinned to the channel walls resulted in greater water accumulation compared to runs without pinning effects and as a result, the standard deviation increased. The observations herein promote the belief that superimposing acoustic pressure waves can be beneficial in terms of removing water droplets from the flow channel. In addition, due to the lowest water accumulation for 80 Hz acoustic vibration, it may be speculated that the majority of water droplets formed in the flow channel have natural frequency of around 80 Hz. Therefore, superimposing acoustic pressure waves at this frequency can induce resonance which eventually enhances water removal from the flow channel. Schafer and Allen[51] also reported that water droplets in flow channels of PEM fuel cells have natural frequencies around 80 Hz.

The effect of pulsating the speaker on and off on water removal has also been studied. This pattern of superimposing acoustic pressure wave is desired as the parasitic power reduces to half compared to runs with continuous operation of the speaker. Fig. 4 shows cumulative area of water droplets in the field of view for two different water flow rates. Each data point is the mean value of three replications and the error bars represent the calculated standard deviation. In addition to lower parasitic power for pulsating mode, it can be inferred from Fig. 4 that pulsating the acoustic vibration can be more effective in removing water from the field of view. For 600 $\mu\ell$/h water flow rate, the cumulative area of water droplet reaches 297.4 and 165.6 mm$^2$ for runs without acoustic vibration and 20 Hz continuous acoustic vibration, respectively, whereas this area reduces to 55.9 mm$^2$ for the speaker pulsating mode at 20 Hz. The same trend can be observed for 400 $\mu\ell$/h water flow rate. However, the cumulative area for the continuous operation mode is relatively closer to the cumulative area in pulsating mode at this water flow rate.

It was observed during the experiment that the majority of water removal in pulsating mode occurred once the speaker was turned on. This can be justified based on the contact angle hysteresis. A static droplet sitting on the surface of the GDL, as shown in Fig. 5a, has a Bond number less than unity. Therefore, capillary forces determine the shape of a static gas-liquid interface. Because the gravitational effects are negligible compared with surface tension effects, the droplet under static condition retains a nearly spherical shape. In Fig. 5a, L, H, and $\theta$ are droplet chord length, droplet height, and static contact angle, respectively. For a droplet under the influence of the core gas flow, as shown in Fig. 5b, the advancing ($\theta_A$) and receding ($\theta_R$) contact angles deform to resist net fluid motion. The difference between advancing and receding contact angles is referred to as the contact angle hysteresis and is an indication of droplet resistance to net motion. A droplet oscillates between advancing and receding contact angles when the acoustic pressure wave is superimposed on the core gas flow, as shown in Fig. 5c. However, for a droplet under the influence of the core gas flow without acoustic pressure wave, turning the speaker on can cause the droplet to transition from the configuration shown in Fig. 5b to the oscillating mode schematically shown in Fig. 5c. Due to the inertia of the pressure wave, the droplet may experience a deformation beyond the contact angle hysteresis and as a result, detachment occurs upon the arrival of the pressure wave to the droplet. Fig. 5d schematically shows the deformation of a droplet beyond its advancing contact angle limit once the speaker turns on.

The oscillating pattern of the droplet was studied by measuring the displacement of the droplet from its emergence point in a test section that allowed side-view visualization. Fig. 6 shows the droplet displacement and side-view area of the droplet as functions of time. The droplet displacement is defined as the horizontal distance between the emergence location and the center of the droplet area in each image. The droplet emerged at 0 s and detached from the surface of the GDL at 140 s. Fig. 6 shows that the droplet was displaced 3 mm on the surface of the GDL from its emergence point prior to detachment. At around 100 s after the emergence, the droplet had over 1 mm displacement in less than four seconds. The oscillating trend in the displacement data points on this figure describes the back and forth movement of the droplet under the influence of the acoustic pressure wave.

***Two-phase flow pressure drop.***—The two-phase flow pressure drop is an in-situ diagnostic tool that reveals information about water accumulation in the flow channel of a PEM fuel cell.[12,59–62] In this study, the two-phase flow pressure drops were measured along 9 cm of the flow channel, as shown in Fig. 7. Fig. 7a shows pressure drop profiles for different conditions tested in this study. It can be observed from the figure that the two-phase flow pressure drop was highest for

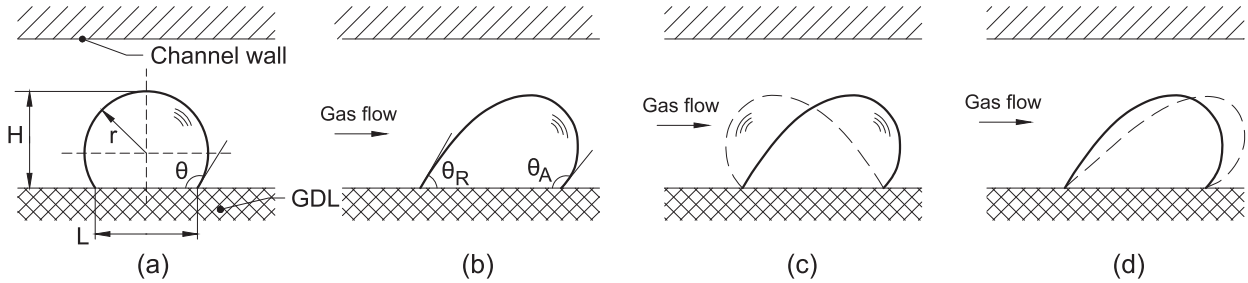


**Figure 5.** Schematic of water droplet (a) in static condition, (b) under the influence of core gas flow, (c) under the influence of the core gas flow superimposed with acoustic pressure wave, (d) under the influence of the core gas flow and upon the arrival of the acoustic pressure wave to the droplet.

the run with no acoustic vibration. This is an indication of the highest water accumulation in the flow channel when the acoustic pressure wave was not superimposed. The first plot in this figure also shows the pressure profile for 80 Hz acoustic vibration. The lower pressure values for this frequency indicate less water accumulation within the flow channel. The pressure drop profiles for other frequencies (20, 40, 60, 100, and 120 Hz) are between the lowest pressure drop (80 Hz) and the highest pressure drop (speaker off mode). Fig. 7b shows the pressure drop readings for 20, 40, and 100 Hz acoustic frequencies. For 20 and 40 Hz, the pressure reading is shown during 1 s of the experiment and for 100 Hz the pressure reading is shown for 0.2 s. For each frequency, Fig. 7b shows that the pressure is oscillating between a lower and upper limit. It can be observed that as the frequency increases, the pressure oscillation decreases. In addition, the figure shows that the number of pressure spikes for each frequency, shown in parentheses, corresponds to the applied frequency. For experiments conducted at 20 and 40 Hz, twenty and forty pressure spikes can be identified, respectively. Similarly, for the experiment conducted at 100 Hz, twenty pressure peaks can be detected during 0.2 s, yielding a hundred pressure peaks during 1 s. Fig. 7c shows the overall two-phase flow pressure drops for different frequencies and averaged for 600 s of the experiment. Each data point is the mean value of three replications and the error bars represent the calculated standard deviation. It can be observed from Fig. 7c that while the highest pressure drop occurred in experiments without acoustic vibration, the lowest pressure drops were obtained in experiments with acoustic vibration. The lowest pressure drop occurred at 80 Hz which confirms findings from cumulative area dta discussed in Fig. 3b. The comparison between Fig. 3b and Fig. 7c shows similarities on cumulative area and pressure drop in flow channel findings. Both figures suggest that the greatest water accumulation occurs when the speaker is off and the lowest water accumulation occurs when the speaker is operating at 80 Hz. In addition, both figures show that water accumulation decreases from the speaker off mode to

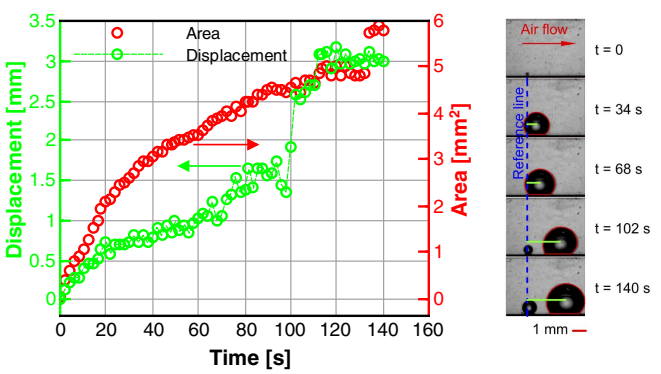


**Figure 6.** Droplet displacement and side-view area from emergence at 0 s to detachment at 140 s. Water flow rate was 2000 $\mu\ell/h$, the superficial air velocity was 1.82 m/s, and the frequency was 20 Hz. The displacement is the length of the green line in images.

80 Hz frequency. The only exception is the cumulative area at 20 Hz which is almost identical to this property at 40 Hz. This may be due to water removal from the field of view while water droplets remained in the part of the flow channel through which the pressure was measured. Moreover, both figures show an increase in water accumulation when the speaker frequency was increased to 100 Hz. The variation of two-phase flow pressure drop based on cumulative water area in the flow channel is shown in Fig. 8. Each data point is the average of three overall pressure drop measurements and the error bars show the standard deviation. The figure shows that the pressure is linearly increasing with cumulative area.

In order to study the validity of pressure drop data obtained during 600 s of experiments, extended experiments were conducted for 3600 s. Fig. 9 shows the pressure drop profiles as well as water droplet area for the three cases of speaker off, speaker on at 20 Hz, and speaker pulsating on and off at 20 Hz. The general trend shown in this figure suggests that pressure drop profiles during 3600 s of experiments are relatively uniform with no significant change with time. For experiment with no acoustic vibration (Fig. 9a) the average pressure drop value over 3600 s was 26.7 Pa. In this figure the pressure drop profile is observed to be between 20 and 40 Pa with few spikes greater than this range. The spikes in pressure data occurred when water build up completely clogged the flow channel. The average pressure drop value over 3600 s with continuous operation of the speaker (Fig. 9b) is 24.9 Pa. While this average pressure drop value is slightly lower than the case with no acoustic vibration, it can be observed that the pressure profile in this figure shows more variation over the entire experiment. For this experiment, the pressure profile shows relatively low pressure at the beginning but it increases up to around 30 Pa at 1000 s. This increase in pressure is then followed by a decrease to lower than 20 Pa at around 1500 s. The pressure drop again increases to over 60 Pa before and after 2000 s which is followed by another decrease at around 2500 s. For the rest of the experiment, the pressure again increases and eventually decreases at the end. Fig. 9b shows the highest standard deviation in pressure drop compared to the other two runs. The pressure profile for the experiment with pulsating operation of the speaker (Fig. 9c) is more uniform compared to the pressure profile for continuous operation of the speaker shown in Fig. 9b. For the pulsating mode, the pressure drop is mostly around 20 Pa with an average of 21.2 Pa for the entire experiment. For each condition in this figure, pressure drop profiles during 60 s of the experiment are shown as well. For the case off case, a drop in pressure profile is observed at approximately 645 s. This drop in pressure is an indication that water has been removed from the length of the flow channel through which the pressure drop was measured. The pressure drop profile for oscillating speaker shows two ranges of pressure, each for 10 s long. The high range of pressure, with values greater than 20 Pa, corresponds to the times when the speaker was on and the low range of pressure, with values less than 20 Pa, corresponds to the times when the speaker was off. Comparison of pressure drop data between the continuous mode and the oscillating mode shows that the latter has a lower standard deviation which reflects a more uniform air flow in the flow channel. In an actual PEM fuel cell this can prevent flow maldistribution in

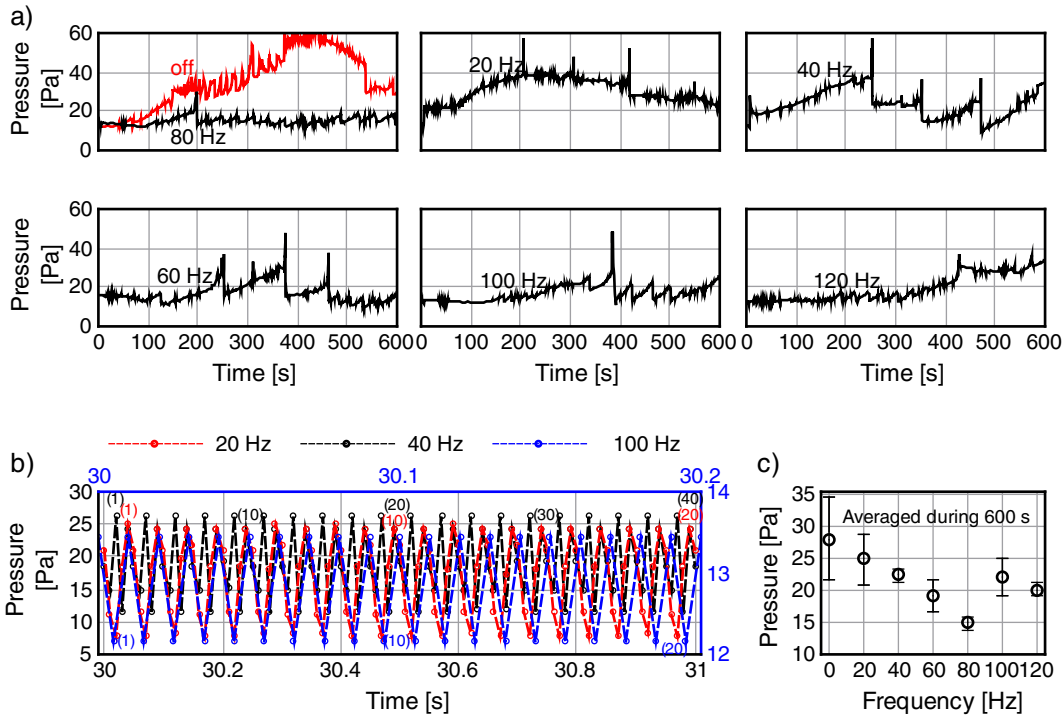


**Figure 7.** Two phase flow pressure drop for 400 μℓ/h water flow rate and 1.82 m/s superficial air velocity measured along 9 cm of the flow channel, (a) at different frequencies and during 600 s, (b) Pressure readings for 20, 40, and 100 Hz acoustic pressure waves. The first two frequencies are plotted with time shown on the bottom axis and the pressure shown on the left axis. The latter frequency is plotted with time shown on the top axis and pressure shown on the right axis, (c) overall pressure drop averaged during 600 s.

parallel flow channels. Liquid water droplet area for extended experiments are also shown in Fig. 9. Fig. 9d shows that the average liquid droplet area is the greatest for the experiment with no acoustic vibration with an average value of 13.35 mm$^2$. This average area is the lowest for the experiment with pulsating operation of the speaker as shown in Fig. 9f. Fig. 9 shows consistency between the average pressure drop and average liquid water droplet area.

Water removal upon speaker activation was studied in separate experiments. In these experiments, referred to as superimposing acoustic pressure wave on demand, the speaker was off by default and turned on manually once a droplet was formed within the flow channel. Fig. 10 shows the pressure drop profiles when the acoustic pressure waves were superimposed on demand. Each pressure spike in this figure indicates a superimposition of acoustic pressure wave on air flow. In most cases, the speaker was on for less than 1 s as figures in the inset indicate. The pressure drop profile for water injection at 400 μℓ/h shows a relatively uniform pressure drop during the entire experiment. This indicates that water removal was accomplished with an appropriate balance with respect to water injection into the flow channel. The same trend can be observed in pressure profile for 600 μℓ/h water injection rate. However, the greater number of pressure spike in this water flow rate indicates that the speaker was turned on more frequently compared to the 400 μℓ/h water flow rate experiment. The number of pressure spikes are greatest for 800 μℓ/h water injection experiment. However, similar to the first two injection flow rates, the pressure profile of 800 μℓ/h water flow rate is relatively uniform over time, suggesting that water did not accumulate within the flow channel during the experiment.

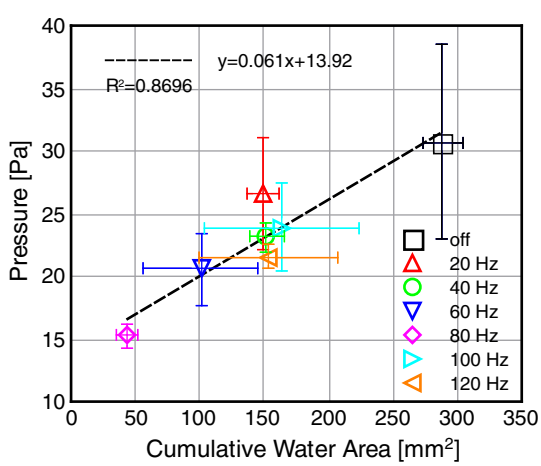


**Figure 8.** Liquid-gas two-phase flow pressure drop based on cumulative area. Water was injected at 400 μℓ/h and the superficial air velocity was 1.82 m/s.

The energy consumed by the speaker to expel each 1 mm$^2$ water droplet for different superimposition scheme is compared by:

$$\text{speaker energy} = \frac{P \cdot t}{A_s - A_a} \quad [1]$$

where P and t are the speaker power and the operation time, respectively. Assuming that water injected to the back side of the GDL enters into the flow channel completely, $A_s$ is the area of supplied water into the flow channel during the length of the experiment. This area is obtained by dividing the volume of water injected during the length of the experiment by the height of the flow channel. $A_a$ is the area of the water droplet accumulated within the flow channel during the experiment which is obtained from flow channel visualization. The difference between $A_s$ and $A_a$ yields the area of water droplet that has been removed from the flow channel. Fig. 11a compares speaker energy consumed for different superimposition scheme. It can be observed from this figure that the speaker used the maximum energy to expel 1 mm$^2$ of water droplet when it was operating continuously throughout the entire experiment. For water flow rates of 400 and 600 μℓ/h, speaker used over 600 J to expel 1 mm$^2$ area of water droplet. However, this energy was reduced to 359.6 J to expel the same area of water droplet when water was injected at 800 μℓ/h. This is because at higher water flow rates

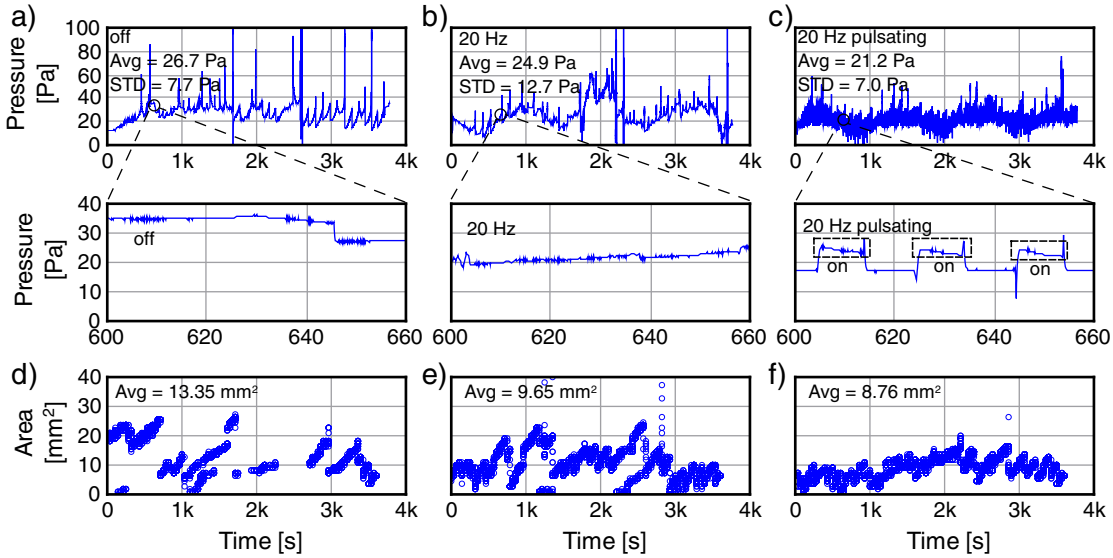


**Figure 9.** Two-phase flow pressure drop and water droplet area in extended experiments (3600 s). Water was injected at 400 μℓ/h and the superficial air velocity was 1.82 m/s. (a) pressure drop for speaker off, (b) pressure drop for speaker continuously on at 20 Hz, (c) pressure drop for speaker pulsating on and off at 20 Hz, (d) liquid water droplet area for speaker off, (e) liquid water droplet area for speaker continuously on, and (f) liquid water droplet area for speaker pulsating on and off.

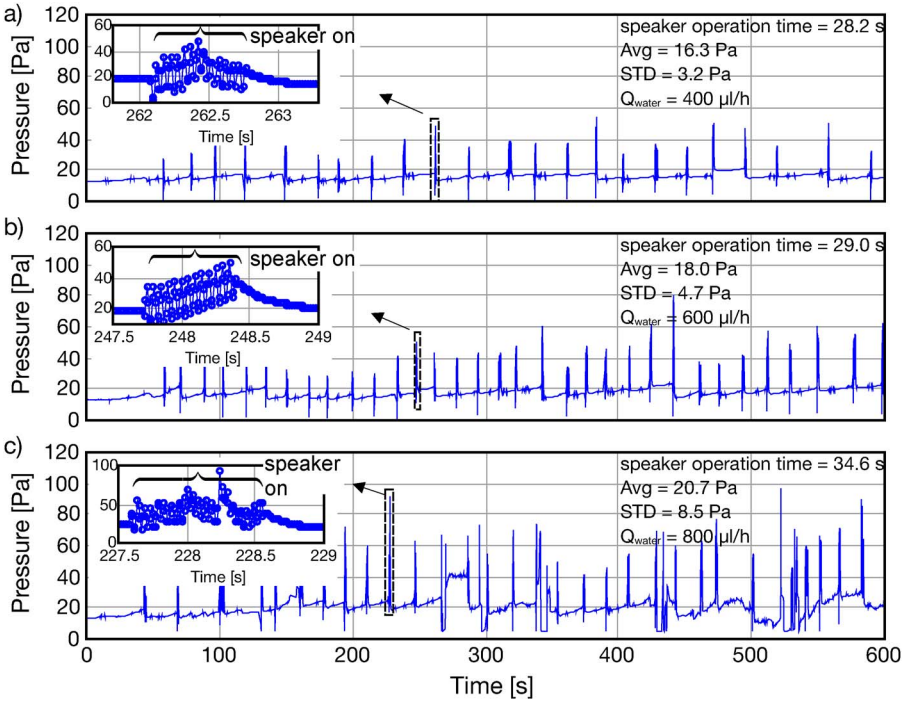


**Figure 10.** Two-phase flow pressure drop profiles for acoustic pressure waves superimposed *on demand*, The superficial air velocity was 1.82 m/s and the speaker frequency was 20 Hz. Water flow rates are (a) 400 (b), 600 and (c) 800 μℓ/h.

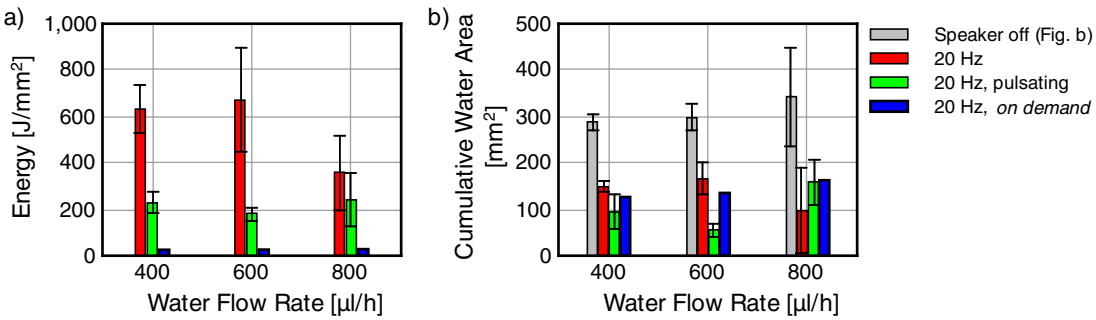


**Figure 11.** Comparison of different superimposition schemes at 1.82 m/s superficial air velocity. (a) Energy consumed by the speaker to remove water droplet, (b) cumulative area.

more water enters into the flow channel and as a result, more excitation from the speaker is required to expel water from the flow channel. The figure shows that pulsating the speaker on and off can save energy to expel water. For all three water flow rates tested in this figure the speaker used around 200 J to expel 1 $mm^2$ area of droplet. The lowest energy consumption belongs to experiments where the speaker was used on demand. For water flow rates of 400, 600, and 800 $\mu\ell$/h, the speaker used 25.6, 26.2, and 28.3 J of energy to expel each 1 $mm^2$ of water droplet area, respectively. Fig. 11b compares cumulative area of water droplets for different conditions. For 400 and 600 $\mu\ell$/h water flow rates, pulsating the speaker on and off outperforms other methods of superimposing acoustic pressure waves. However, for the highest water flow rate tested in this study, having the speaker continuously on removes the maximum amount water from the flow channel. For this water flow rate, however, pulsating the speaker on and off yields similar water removal as applying acoustic pressure wave on demand.

While this study demonstrated the ability of acoustic pressure waves to reduce water buildup in single PEM fuel cell flow channel, this enhanced water removal technique can still be applied on fuel cell stacks where single cells are connected in parallel. One potential approach to apply this technique in a fuel cell stack is to superimpose acoustic pressure waves into each individual cell by placing acoustic wave sources at each cell inlet within the stack manifold. Alternatively, a single acoustic pressure wave source in a manifold with enough intensity may be enough to affect all the cells in the stack. The authors are in the midst of testing the latter technique on an in-situ single cell where multiple channels are connected via a single manifold. In addition, the authors are currently evaluating the effectiveness of this technique in removing water in anode side. This is because the lower anode flow rates and the lower density of hydrogen make droplet removal difficult.[63,64]

The findings from this study showed that superimposing acoustic pressure waves on air flow can be beneficial in terms of expelling water droplets from inside the flow channels. The novelty of the present work with respect to the previously published studies such as Refs. 51,52 include; (*i*) testing a wider range of frequencies, (*ii*) superimposing acoustic pressure waves in pulsating as well as on demand mode, (*iii*) incorporating pressure drop data, (*iv*) evaluating cumulative area as a function of time, and (*v*) evaluating droplet displacement from a side-view angle. Because the natural frequency of a water droplet depends on its size and considering the fact that in an actual PEM fuel cell droplets with different sizes form on the surface of GDL, testing a wide range of frequencies was necessary to identify the desired frequency that yields the greatest water removal. In addition, while only a continuous mode of superimposing was tested in Refs. 51,52, novel superimposing modes such as pulsating and/or on demand proved to be more efficient in terms of speaker energy used to expel the same area of water droplet.

## Conclusions

Enhanced water removal from the flow channel of an ex-situ PEM fuel cell test section was achieved by inducing resonance in water droplets at their natural frequencies. Acoustic pressure waves were superimposed on air flow and water removal at different frequencies was visualized with a CCD camera. Cumulative area of water droplets in the flow channel was obtained based on image processing. In addition, liquid-gas two-phase flow pressure drop was measured along the flow channel. The oscillation of water droplet was also observed from a side-view angle in a goniometer. The following conclusions can be drawn from this study:

1. Superimposing acoustic pressure wave on air flow is beneficial in terms of removing water droplets from the flow channel. Among different frequencies tested in this study, 80 Hz proved to remove the greatest amount of water. While an average water cumulative area as high as 288.6 $mm^2$ was obtained for runs without acoustic vibration, this average was reduced to 43.9 $mm^2$ for runs with 80 Hz acoustic pressure waves. The small standard deviation in the cumulative area plot for this frequency indicates a similar trend in the three runs conducted.
2. For higher frequencies tested in this study (100 and 120 Hz), it was observed that as water droplet pins to the channel side walls, it can be barely removed from the flow channel. This is because droplets tend to grow in size in pinning locations which lowers their natural frequencies and as a result, the higher range of frequencies tested were not capable of removing them. However, proper water removal was observed for the same frequencies when water droplet did not pin to the channel side walls. This justifies the relatively large standard deviation observed in the cumulative area plot for 100 and 120 Hz.
3. Pulsating the speaker on and off was observed to expel more water from the flow channel when water was injected at 400 and 600 $\mu\ell$/h. However, having the speaker continuously on for 800 $\mu\ell$/h water flow rate experiment proved to expel more water from the flow channel. It was observed that the majority of water droplets were removed once the speaker was turned on.
4. Water droplet oscillation under the influence of acoustic pressure wave was observed from a side-view angle through experiments conducted in a goniometer. Analyzing images showed a 3-mm displacement in water droplet due to acoustic vibration from the emergence location to the detachment location. In addition the contact angle hysteresis was obtained based on droplet's oscillations between the advancing and receding contact angles.
5. The two-phase flow pressure drops indicated the lowest water accumulation for 80 Hz acoustic vibration while the water accumulation was highest for runs without acoustic vibration. The overall two-phase flow pressure drops decreased from 0 Hz (no acoustic vibration) to 80 Hz. However, increasing the frequency to 100 Hz increased the two-phase flow pressure drop. In addition, the two-phase flow pressure drop was observed to increase linearly with cumulative area of water droplets in the flow channel.
6. A comparison between speaker energy consumed at different superimposition schemes suggested that the on demand pattern was the most efficient scheme in terms of parasitic power. In this pattern, the speaker was mainly off and the acoustic vibration was applied once the droplet was emerged from the surface of the GDL. Findings from Fig. 11 suggest that for water injection rate of 400 $\mu\ell$/h while 631.9 J was required to expel 1 $mm^2$ area of the water droplet for a continuous operation of the speaker, only 25.6 J of energy was used to expel the same area of water droplet when the acoustic pressure wave was superimposed on demand. The energy required to expel the same area of water droplet was 227.6 J when the speaker was operating in a pulsating mode with 10 intervals.

It should be added that while these results are obtained based on an ex-situ approach in a scaled-up flow channel, the findings can still be used to successfully remove water from the flow channels of a PEM fuel cell. The lower water accumulation at 80 Hz compared to runs without acoustic vibration, for instance, can be exploited to alleviate the flooding issue in PEM fuel cell flow channels. Similarly, superimposing acoustic pressure waves with an on demand approach can be a potential remedy to remove water droplets from the flow channels while keeping parasitic powers low. This method of superimposing acoustic vibration requires operating of the speaker at the correct time, once droplet forms within the flow channel. The formation of water droplet in flow channel can be detected by measuring the liquid-gas two-phase flow pressure drop. Therefore, the two-phase flow pressure drop measurements can be the input of the controller that controls the operation of the speaker in such systems.

## Acknowledgments

Western New England University is gratefully acknowledged for supporting this project. The authors also thank Matthew Musiak for assisting in measuring the speaker power and Peter Bennett for fabricating the test sections used in this study.

## ORCID

Mehdi Mortazavi https://orcid.org/0000-0002-2222-8044
Anthony D. Santamaria https://orcid.org/0000-0001-6410-8510
Jingru Z. Benner https://orcid.org/0000-0002-8173-4828
Vedang Chauhan https://orcid.org/0000-0001-8807-962X

## References

1. Adam Z. Weber, Rodney L. Borup, Robert M. Darling, Prodip K. Das, Thomas J. Dursch, Wenbin Gu, David Harvey, Ahmet Kusoglu, Shawn Litster, Matthew M. Mench, Rangachary Mukundan, Jon P. Owejan, Jon G. Pharoah, Marc Secanell, and Iryna V. Zenyuk, A critical review of modeling transport phenomena in polymer-electrolyte fuel cells, *Journal of The Electrochemical Society*, **161**(12), F1254 (2014).
2. P. Satjaritanun, S. Hirano, A. Shum, I. Zenyuk, A. Weber, J. Weidner, and S. Shimpalee, Fundamental Understanding of Water Movement in Gas Diffusion Layer under Different Arrangements Using Combination of Direct Modeling and Experimental Visualization, *Journal of The Electrochemical Society*, **165**(13), F1115 (2018).
3. M. Perry and T. Fuller, A Historical Perspective of Fuel Cell Technology in the 20th Century, *Journal of The Electrochemical Society*, **149**(7), S59 (2002).
4. Y. Wang, K. S. Chen, J. Mishler, S. C. Cho, and X. C. Adroher, A review of polymer electrolyte membrane fuel cells: Technology, applications, and needs on fundamental research, *Applied Energy*, **88**, 981 (2010).
5. A. Faghri and Z. Guo, Challenges and Opportunities of Thermal Management Issues Related to Fuel Cell Technology and Modeling, *International Journal of Heat and Mass Transfer*, **48**, 3891 (2005).
6. R. Borup, J. Meyers, B. Pivovar, Y. S. Kim, R. Mukundan, N. Garland, D. Myers, M. Wilson, F. Garzon, and D. Wood et al, Scientific aspects of polymer electrolyte fuel cell durability and degradation, *Chemical Reviews*, **107**, 3904 (2007).
7. M. A. Hickner, N. P. Siegel, K. S. Chen, D. S. Hussey, and D. L. Jacobson, Observations of Transient Flooding in a Proton Exchange Membrane Fuel Cell Using Time-Resolved Neutron Radiography, *Journal of The Electrochemical Society*, **157**, B32 (2010).
8. T. E. Springer, T. A. Zawodzinski, and S. Gottesfeld, Polymer electrolyte fuel cell model, *Journal of the Electrochemical Society*, **138**(8), 2334 (1991).
9. T. A. Zawodzinski, T. E. Springer, J. Davey, R. Jestel, C. Lopez, J. Valerio, and S. Gottesfeld, Comparative study of water uptake by and transport through ionomeric fuel cell membranes, *Journal of the Electrochemical Society*, **140**(7), 1981 (1993).
10. U. Pasaogullari and C. Y. Wang, Liquid water transport in gas diffusion layer of polymer electrolyte fuel cells, *Journal of the Electrochemical Society*, **151**, A399 (2004).
11. J. Ihonen, M. Mikkola, and G. Lindbergh, Flooding of gas diffusion backing in PEFCs physical and electrochemical characterization, *Journal of the Electrochemical Society*, **151**, A1152 (2004).
12. I. S. Hussaini and C. Y. Wang, Visualization and quantification of cathode channel flooding in PEM fuel cells, *Journal of Power Sources*, **187**, 444 (2009).
13. K. Tuber, D. Pocza, and C. Hebling, Visualization of water buildup in the cathode of a transparent PEM fuel cell, *Journal of Power Sources*, **124**, 403 (2003).
14. X. Liu, H. Guo, and C. Ma, Water flooding and two-phase flow in cathode channels of proton exchange membrane fuel cells, *Journal of Power Sources*, **156**, 267 (2006).
15. T. Fabian, R. O'Hayre, S. Litster, F. B. Prinz, and J. G. Santiago, Passive water management at the cathode of a planar air-breathing proton exchange membrane fuel cell, *Journal of Power Sources*, **195**(10), 3201 (2010).
16. A. Santamaria, H. Y. Tang, J. W. Park, G. G. Park, and Y. J. Sohn, 3D neutron tomography of a polymer electrolyte membrane fuel cell under sub-zero conditions, *International Journal of Hydrogen Energy*, **37**(14), 10836 (2012).
17. J. J. Kowal, A. Turhan, K. Heller, J. Brenizer, and M. M. Mench, Liquid water storage, distribution, and removal from diffusion media in PEFCS, *Journal of the Electrochemical Society*, **153**(10), A1971 (2006).
18. A. D. Santamaria, J. Bachman, and J. W. Park, Cold-start of parallel and interdigitated flow-field polymer electrolyte membrane fuel cell, *Electrochimica Acta*, **107**, 327 (2013).
19. A. Taniguchi, T. Akita, K. Yasuda, and Y. Miyazaki, Analysis of electrocatalyst degradation in PEMFC caused by cell reversal during fuel starvation, *Journal of Power Sources*, **130**, 42 (2004).
20. J. T. Gostick, M. A. Ioannidis, M. W. Fowler, and M. D. Pritzker, Direct measurement of the capillary pressure characteristics of water-air-gas diffusion layer systems for PEM fuel cells, *Electrochemistry Communications*, **10**, 1520 (2008).
21. J. T. Gostick, M. A. Ioannidis, M. W. Fowler, and M. D. Pritzker, Wettability and capillary behavior of fibrous gas diffusion media for polymer electrolyte membrane fuel cells, *Journal of Power Sources*, **194**, 433 (2009).
22. S. Litster, D. Sinton, and N. Djilali, Ex situ visualization of liquid water transport in PEM fuel cell gas diffusion layers, *Journal of Power Sources*, **154**, 95 (2006).
23. I. V. Zenyuk, D. Y. Parkinson, G. Hwang, and A. Z. Weber, Probing water distribution in compressed fuel-cell gas-diffusion layers using X-ray computed tomography, *Electrochemistry Communications*, **53**, 24 (2015).
24. I. V. Zenyuk, A. Lamibrac, J. Eller, D. Parkinson, F. Marone, F. Buchi, and A. Z. Weber, Investigating evaporation in gas diffusion layers for fuel cells with X-ray computed tomography, *The Journal of Physical Chemistry C*, **120**(50), 28701 (2016).
25. K. Jiao, J. Park, and X. Li, Experimental investigations on liquid water removal from the gas diffusion layer by reactant flow in a PEM fuel cell, *Applied Energy*, **87**, 2770 (2010).
26. A. D. Santamaria, P. K. Das, J. C. MacDonald, and A. Z. Weber, Liquid-water interactions with gas-diffusion-layer surfaces, *Journal of The Electrochemical Society*, **161**(12), F1184 (2014).
27. J. Park, H. Oh, Y. Lee, K. Min, E. Lee, and J. Y. Jyoung, Effect of the pore size variation in the substrate of the gas diffusion layer on water management and fuel cell performance, *Applied Energy*, **171**, 200 (2016).
28. H. Y. Tang, A. D. Santamaria, J. Bachman, and J. W. Park, Vacuum-assisted drying of polymer electrolyte membrane fuel cell, *Applied energy*, **107**, 264 (2013).
29. M. Mortazavi and K. Tajiri, In-Plane Microstructure of Gas Diffusion Layers With Different Properties for PEFC, *Journal of Fuel Cell Science and Technology*, **11**, 021002 (2014).
30. A. M. Pivovar and B. S. Pivovar, Dynamic behavior of water within a polymer electrolyte fuel cell membrane at low hydration levels, *The Journal of Physical Chemistry B*, **109**, 785 (2005).
31. B. S. Pivovar, An overview of electro-osmosis in fuel cell polymer electrolytes, *Polymer*, **47**, 4194 (2006).
32. A. Bazylak, D. Sinton, and N. Djilali, Dynamic water transport and droplet emergence in PEMFC gas diffusion layers, *Journal of Power Sources*, **176**, 240 (2008).
33. P. K. Das, X. Li, and Z. S. Liu, Analysis of liquid water transport in cathode catalyst layer of PEM fuel cells, *International Journal of Hydrogen Energy*, **35**(6), 2403 (2010).
34. M. Mortazavi and K. Tajiri, Liquid water breakthrough pressure through gas diffusion layer of proton exchange membrane fuel cell, *International Journal of Hydrogen Energy*, **39**(17), 9409 (2014).
35. E. F. Medici and J. S. Allen, Scaling percolation in thin porous layers, *Physics of Fluids*, **23**(12), 122107 (2011).
36. J. P. Owejan, J. E. Owejan, W. Gu, T. A. Trabold, T. W. Tighe, and M. F. Mathias, Water Transport Mechanisms in PEMFC Gas Diffusion Layers, *Journal of the Electrochemical Society*, **157**, B1456 (2010).
37. T. F. Fuller and J. Newman, Experimental determination of the transport number of water in Nafion 117 membrane, *Journal of The Electrochemical Society*, **139**(5), 1332 (1992).
38. E. F. Medici and J. S. Allen, The effects of morphological and wetting properties of porous transport layers on water movement in PEM fuel cells, *Journal of The Electrochemical Society*, **157**, B1505 (2010).
39. N. J. Cooper, A. D. Santamaria, M. K. Becton, and J. W. Park, Neutron radiography measurements of in-situ PEMFC liquid water saturation in 2D and 3D morphology gas diffusion layers, *International Journal of Hydrogen Energy*, **42**, 16269 (2017).
40. E. F. Medici and J. S. Allen, Evaporation, two phase flow, and thermal transport in porous media with application to low-temperature fuel cells, *International Journal of Heat and Mass Transfer*, **65**, 779 (2013).
41. F. Y. Zhang, X. G. Yang, and C. Y. Wang, Liquid Water Removal From A Polymer Electrolyte Fuel Cell, *Journal of the Electrochemical Society*, **153**, A225 (2006).
42. M. Mortazavi and M. Tajiri, Effect of the PTFE content in the gas diffusion layer on water transport in polymer electrolyte fuel cells (PEFCs), *Journal of Power Sources*, **245**, 236 (2014).
43. J. P. Owejan, J. J. Gagliardo, S. R. Falta, and T. A. Trabold, Accumulation and removal of liquid water in proton exchange membrane fuel cells, *Journal of The Electrochemical Society*, **156**, B1457 (2009).
44. P. K. Das, A. Grippin, A. Kwong, and A. Z. Weber, Liquid-Water-Droplet Adhesion-Force Measurement on Fresh and Aged Fuel-Cell Gas-Diffusion Layers, *J. Electrochemical Society*, **159**, 489 (2012).
45. J. Bachman, M. Charvet, A. Santamaria, H. Y. Tang, J. W. Park, and R. Walker, Experimental investigation of the effect of channel length on performance and water accumulation in a PEMFC parallel flow field, *International Journal of Hydrogen Energy*, **37**(22), 17172 (2012).
46. A. D. Santamaria, MaxM. K. Becton, N. J. Cooper, A. Z. Weber, and J. W. Park, Effect of cross-flow on PEFC liquid-water distribution: An in-situ high-resolution neutron radiography study, *Journal of Power Sources*, **293**, 162 (2015).
47. R. Finn, Introduction, *Equilibrium Capillary Surfaces*, 1 (1986).
48. M. M. Weislogel and S. Lichter, Capillary flow in an interior corner, *Journal of Fluid Mechanics*, **373**, 349 (1998).
49. Allen, J. S. Son, and S. Collicot, Proton exchange membrane fuel cell flow field desing for improved water management, *Handbook of Fuel Cells*, 1 (2010).
50. V. Palan, W. S. Shepard Jr, and K. A. Williams, Removal of excess product water in a PEM fuel cell stack by vibrational and acoustical methods, *Journal of Power Sources*, **161**(2), 1116 (2006).
51. A. M. Schafer and J. S. Allen, Improved water removal from fuel cell flow channels via natural frequency excitation of free surfaces, *ECS Transactions*, **41**(1), 1, 1887 (2011).
52. Andrew M. Schafer, *A Technique for Improved Water Removal from PEM Fuel Cells via Natural Frequency Excitation of Free Surfaces*, M.S. Thesis, Michigan Technological University, 2010.
53. C. P. Migliaccio, Resonance-induced condensate shedding for high-efficiency heat transfer, *International Journal of Heat and Mass Transfer*, **79**, 720 (2014).
54. H. Y. Kim, Drop fall-off from the vibrating ceiling, *Physics of Fluids*, **16**(2), 474 (2004).
55. Y. Choe and E. S. Kim, Valveless micropump driven by acoustic streaming, *Journal of Micromechanics and Microengineering*, **23**(4), 045005 (2013).
56. Y. N. Cheung, N. T. Nguyen, and T. N. Wong, Droplet manipulation in a microfluidic chamber with acoustic radiation pressure and acoustic streaming, *Soft Matter*, **10**(40), 8122 (2014).

57. M. Mathias, J. Roth, J. Fleming, and W. Lehnert, Handbook of Fuel Cells-Fundamentals, Technology and Applications, Vol. 3: Fuel Cell Technology and Application, NY: John Wiley & Sons, 517, 2003.
58. C. M. Hwang, M. Ishida, H. Ito, T. Maeda, A. Nakano, Y. Hasegawa, N. Yokoi, A. Kato, and T. Yoshida, Influence of properties of gas diffusion layers on the performance of polymer electrolyte-based unitized reversible fuel cells, *International Journal of Hydrogen Energy*, **36**, 1740 (2010).
59. M. Mortazavi and K. Tajiri, Two-phase flow pressure drop in flow channels of proton exchange membrane fuel cells: Review of experimental approaches, *Renewable and Sustainable Energy Reviews*, **45**, 296 (2015).
60. J. S. Allen, Two phase flow in small channels and the implications for PEM feul cell operation, *ECS Transactions*, **3**, 1197 (2006).
61. R. Anderson, L. Zhang, Y. Ding, M. Blanco, X. Bi, and D. P. Wilkinson, A critical review of two-phase flow in gas flow channels of proton exchange membrane fuel cells, *Journal of Power Sources*, **195**(15), 4531 (2010).
62. R. Anderson, E. Eggleton, and L. Zhang, Development of two-phase flow regime specific pressure drop models for proton exchange membrane fuel cells, *International Journal of Hydrogen Energy*, **40**(2), 1173 (2015).
63. Iryna V. Zenyuk, Prodip K. Das, and Adam Z. Weber, Understanding Impacts of Catalyst-Layer Thickness on Fuel-Cell Performance via Mathematical Modeling, *Journal of The Electrochemical Society*, **163**(7), F691 (2016).
64. Iryna V. Zenyuk, Dilworth Y. Parkinson, Liam G. Connolly, and Adam Z. Weber, Gas-diffusion-layer structural properties under compression via X-ray tomography, *Journal of Power Sources*, **328**, 364 (2016).